

# 中国激光

## 激光薄膜元件内微缺陷的表征分析

崔云<sup>1,2\*</sup>, 张革<sup>1,2</sup>, 赵元安<sup>1,2</sup>, 邵宇川<sup>1,2</sup>, 朱美萍<sup>1,2</sup>, 易葵<sup>1,2</sup>, 邵建达<sup>1,2\*\*</sup>

<sup>1</sup>中国科学院上海光学精密机械研究所薄膜光学实验室, 上海 201800;

<sup>2</sup>中国科学院强激光材料重点实验室, 上海 201800

**摘要** 激光系统用薄膜元件既要有优异的光学性能, 又要有高的激光诱导损伤阈值(LIDT)。薄膜元件的基底表面上交替沉积有高低折射率材料, 通过膜厚、折射率等参数的优化可实现所需的光学性能, 但元件中存在的微缺陷(如膜料喷溅缺陷、基底缺陷等)是导致LIDT降低的重要原因。通过精准定位切割、三维重构的方法, 表征膜料喷溅和基底抛光产生的微缺陷的形貌结构, 并对其激光辐照前后的元素分布进行了分析。研究结果为镀制工艺、基底加工工艺的改进提供了参考。

**关键词** 薄膜; 激光损伤; 微缺陷; 喷溅; 基底抛光

中图分类号 O439

文献标志码 A

DOI: 10.3788/CJL220568

### 1 引言

激光薄膜元件在许多激光系统中发挥着重要作用, 包括惯性约束聚变(ICF)激光器<sup>[1-3]</sup>、超短超快激光器<sup>[4]</sup>、高功率光纤激光器<sup>[5-6]</sup>等。快速发展的高功率激光技术对激光系统中的薄膜元件提出了更高的要求, 不仅要求其具有优良的光学性能, 更要求其具有高抗激光辐照能力。用于紫外-近红外(UV-NIR)波段、纳秒级激光系统的薄膜元件的基底表面上交替沉积有高低折射率材料, 特别是在532 nm、355 nm激光系统<sup>[7-8]</sup>中, HfO<sub>2</sub>和SiO<sub>2</sub>薄膜材料由于较低的紫外截止边和较高的带隙而得到广泛应用<sup>[9-10]</sup>。通常采用电子束蒸发的方式制备薄膜元件, 其中对激光诱导损伤阈值(LIDT)影响较大的微缺陷包括膜料喷溅缺陷和基底缺陷。为了控制微缺陷, 首先要找到缺陷<sup>[11]</sup>并分析其来源, 针对这两类微缺陷国内外都展开了相关研究。

膜料喷溅缺陷产生的原因是电子束属于点蒸发源, 在蒸发膜料过程中产生的宽沉积羽流会发生喷溅<sup>[12]</sup>, 喷溅产生的缺陷被包埋在膜层内, 大部分呈节瘤状, 因此也被称为节瘤缺陷<sup>[13-14]</sup>。其基本形貌特征是膜料喷溅在薄膜内部形成一个种子核, 由于自阴影效应, 后续膜层逐渐堆积在种子核上形成一个与规整膜层间有明显结构性边界的三维倒锥形结构体, 其直径会随着厚度的增加而增加, 在膜层表面上的表现是一个球冠状结构<sup>[15]</sup>。节瘤缺陷直径越大, 节瘤缺陷内的光增强收集区域就越大; 节瘤缺陷越深, 结合力越

强, 喷射时产生的附带损伤越大, 开裂和损伤程度越大<sup>[13]</sup>。节瘤缺陷的纳秒激光损伤模型主要是热力损伤模型<sup>[16]</sup>, 该模型基于节瘤的场增强效应, 部分激光能量在种子区沉积, 导致种子区迅速升温并通过热传导在周围材料中形成一个随时间变化的温度梯度场, 最终形成动态热应力场。在应力的作用下, 高温的种子区周围产生微裂纹, 这是破坏开始的临界状态, 与该状态对应的人射激光能流密度被定义为损伤阈值, 损伤形貌与节瘤处的电场强度呈现出较好的对应关系<sup>[17]</sup>。

基底缺陷主要是在研磨、抛光过程中在基底亚表面层引入的坑点、划痕或裂纹。通过在熔石英基底表面上制作人工机械划痕并直接镀制高反膜<sup>[18]</sup>, 发现不同尺寸划痕对薄膜生长有不同影响。坑点、划痕或裂纹中藏匿着吸收性杂质, 划痕表面的悬挂键也会吸附环境中的杂质。杂质吸收激光、划痕或裂纹同时增强电场<sup>[19-20]</sup>是导致元件抗激光损伤能力降低的主要因素<sup>[21-22]</sup>。为了去除基底缺陷, 研究人员采用不同处理程序(如超声清洗、酸溶液蚀刻)<sup>[23-24]</sup>对基底进行处理。超声清洗过程是包括Al<sub>2</sub>O<sub>3</sub>抛光液擦洗、温和清洗剂超声清洗、纯水冲洗、去离子水超声清洗等几个步骤的组合。这种方法的好处是简单快捷地去除表面杂质, 不会引入二次杂质污染。但这种方法无法有效地去除亚表面坑点、划痕或裂纹缺陷, 甚至会将更多的亚表面缺陷暴露出来。抛光液的主要成分也容易留在亚表面缺陷内。酸溶液蚀刻虽然可以有效去除亚表面缺陷, 但同时会导致表面粗糙度变差、面形

收稿日期: 2022-02-14; 修回日期: 2022-03-04; 录用日期: 2022-05-06; 网络首发: 2022-05-16

基金项目: 国家自然科学基金(61975215)

通信作者: \*cuiyun@siom.ac.cn; \*\*jdshao@mail.shcnc.ac.cn

畸变。

综上所述,通过找到薄膜元件的微缺陷、分析其来源并研究该缺陷在高能激光作用下的损伤特征,可以溯源微缺陷形成的工艺环节,完善激光与物质相互作用的损伤机制,明确薄膜元件激光损伤阈值提升的方向。本文主要对微米及亚微米(百纳米)量级的微缺陷进行了表征分析。

## 2 样品制备和测试手段

### 2.1 样品制备

本文使用 355 nm 和 532 nm 高反膜作为研究对象,使用电子束蒸发技术将  $\text{HfO}_2$ 、 $\text{SiO}_2$  膜层交替沉积在 BK7 基底上,膜系结构如图 1 所示。其中,H,L 分别代表光学厚度为  $\frac{\lambda}{4}$ ( $\lambda$  为光波长)的高( $\text{HfO}_2$ )、低( $\text{SiO}_2$ )折射率层, $xL$  和  $yL$  分别对应过渡层和保护层, $x$  和  $y$  的值在 0~4 之间。镀膜前,镀膜室加热至 200 °C,本底真空抽至压强优于  $1 \times 10^{-3}$  Pa; 镀膜过程中, $\text{HfO}_2$  和  $\text{SiO}_2$  的沉积速率为 0.1 nm/s 和 0.2 nm/s。

### 2.2 测试手段

使用带聚焦离子束(FIB)的扫描电子显微镜(SEM)观察微缺陷形貌,使用离子束切割特征点获取截面形貌和结构,并与能量色散光谱仪(EDS)相结合,分析指定区域的元素组成。

使用加速电压值为 200 keV 的场发射透射电子显微镜(TEM)获得微缺陷的明场像及扫描透射电子显微镜-高角度环形暗场(STEM-HAADF)像,并结合

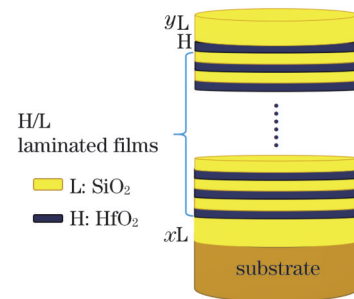


图 1 355 nm/532 nm 高反膜结构示意图

Fig. 1 Structural diagram of 355 nm/532 nm high-reflection film

EDS 获得样品的成分信息,采用三维重构的方式对微缺陷进行立体分析。使用 FIB 制备用于 TEM 观察的样品。

采用 1-on-1 方式进行 LIDT 测试,二倍频( $2\omega$ ) Nd:YAG 激光器出射脉冲宽度为 8 ns 的 532 nm 激光,样品表面的有效光束尺寸约为  $0.32 \text{ mm}^2$ ,三倍频( $3\omega$ ) Nd:YAG 激光器出射脉冲宽度为 8 ns 的 355 nm 激光,样品表面的有效光束尺寸约为  $0.30 \text{ mm}^2$ 。在每个能量台阶下测试 10 个点。

## 3 测试结果和讨论

### 3.1 膜料喷溅微缺陷的表征

镀膜元件表面由于膜料喷溅形成的典型节瘤缺陷如图 2 所示,微米量级的节瘤缺陷的球冠尺寸较大,如图 2(a)所示,种子源也较大,如图 2(b)、(c)所示,截面图中亮色区域为  $\text{HfO}_2$ ,暗色区域为  $\text{SiO}_2$ ,表明节瘤种子既有  $\text{HfO}_2$  也有  $\text{SiO}_2$ 。

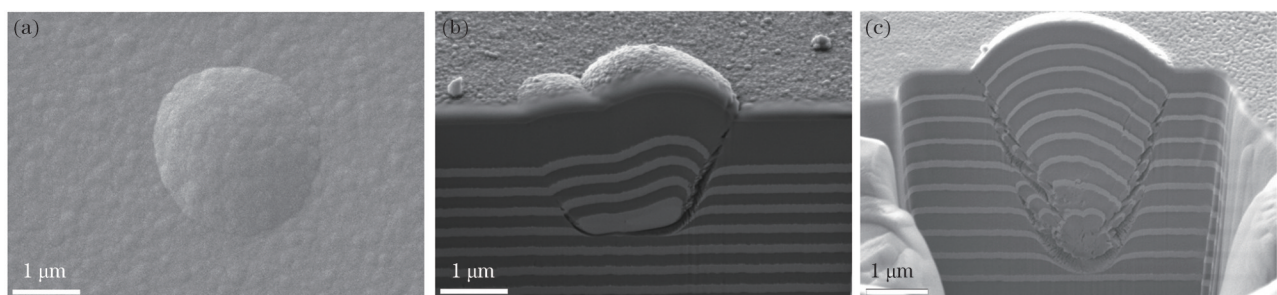


图 2 膜料喷溅产生的微米量级节瘤缺陷的 SEM 图。(a) 薄膜表面典型节瘤形貌;(b) 节瘤内  $\text{HfO}_2$  种子;(c) 节瘤内  $\text{SiO}_2$  种子  
Fig. 2 SEM images of micron-scale nodule defects produced by film material ejection. (a) Typical nodule morphology on film surface;

(b)  $\text{HfO}_2$  seed in nodule; (c)  $\text{SiO}_2$  seed in nodule

亚微米量级节瘤缺陷在薄膜表面上的尺寸较小,如图 3(a)所示,球冠直径近 800 nm,其种子源更小,且没有明显的结构性边界,很难再用聚焦离子束(FIB)切割的方式确定种子源的位置和成分,如图 3(b)、(c)所示。

因此,以亚微米量级节瘤为中心,将缺陷切成类圆柱体,采用 TEM 三维重构的方式,对亚微米量级节瘤进行分析,最终发现其种子源尺寸为 100 nm,如图 4 所示。图 4(a)、(b) 分别为三维重构的正面图和侧面图。

用 TEM 对圆柱体进行 HAADF 成像,如图 5(a)所示。用 EDS 对圆柱体进行与 HAADF 像对应的成分分析,测得种子源位置处的成分为 Si 和 O,如图 5(b)~(d) 所示,证实其种子源为喷溅的  $\text{SiO}_2$ ,位于  $xL$  打底层中。除膜层中的 Hf、Si、O 元素外,在基底和  $\text{HfO}_2$  层中发现了 Na、K 离子的富集,如图 5(e)、(f) 所示。这是由于 BK7 基底含有少量 Na、K 离子,在镀膜过程中,加温和真空的共同作用使得来自基底的 Na、K 离子扩散并聚集在高折射率膜层中<sup>[25-26]</sup>。

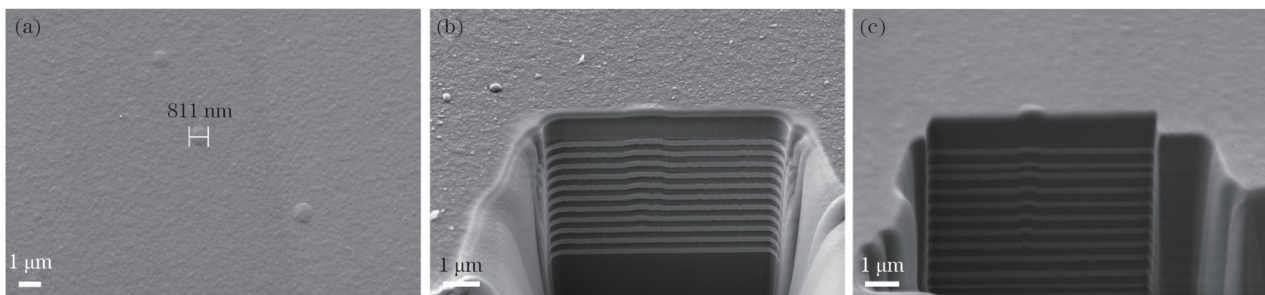


图3 膜料喷溅产生的亚微米量级节瘤缺陷的SEM图。(a)薄膜表面典型节瘤形貌;(b)一个节瘤缺陷的截面;(c)另一个节瘤缺陷的截面

Fig. 3 SEM images of submicron nodule defects produced by film material ejection. (a) Typical nodule morphology on film surface; (b) section of a nodule defect ; (c) section of another nodule defect

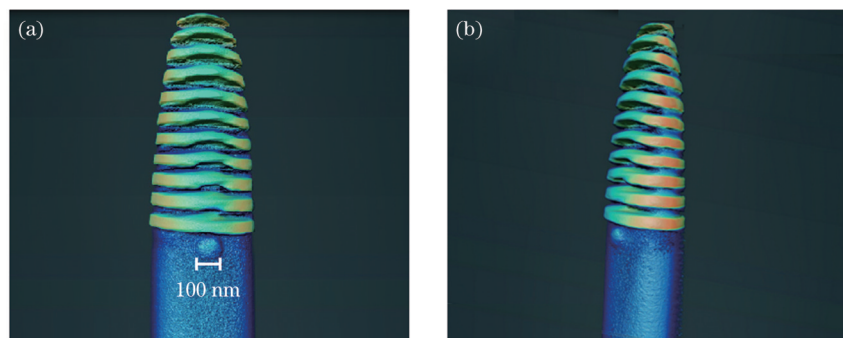


图4 亚微米量级节瘤缺陷的TEM三维重构图。(a)正视;(b)侧视  
Fig. 4 TEM 3D reconstruction views of submicron nodule defect. (a) Front view; (b) side view

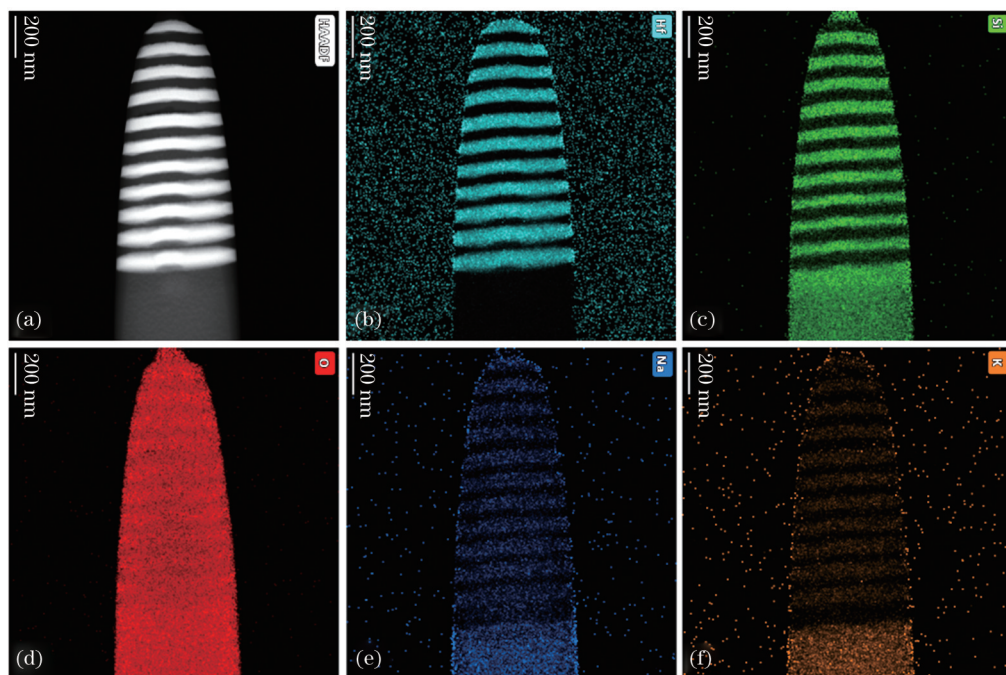


图5 TEM-EDS测得的亚微米量级节瘤缺陷中的元素分布。(a)HAADF像;(b)Hf;(c)Si;(d)O;(e)Na;(f)K

Fig. 5 Element distributions in submicron nodule defects measured by TEM-EDS. (a) HAADF image; (b) Hf; (c) Si; (d) O; (e) Na; (f) K

### 3.2 基底表面缺陷的表征

对传统抛光基底表面进行形貌观察,发现了基底抛光过程中产生的坑点和微裂纹,如图6所示;对基底进行200 °C退火后基底微裂纹处析出浅色类球状杂质,如图6(b)所示。在这样的抛光基底上镀

膜,并在基底缺陷对应位置上对镀制的薄膜进行FIB切割,在截面上可以看到基底缺陷导致的膜层剥离和孔隙,如图7(a)所示;较大的基底杂质也会导致类节瘤缺陷结构,如图7(b)所示。这是由于镀膜过程中的温度为200 °C,且处于真空环境,因此镀膜

过程中基底缺陷的放气和杂质析出对膜层产生影响。对图 7(b)中的基底杂质进行元素分布分析,发现基底杂质的成分主要为 Al 和 O,如图 8 所示,这应该

是基底抛光过程中使用的  $\text{Al}_2\text{O}_3$  抛光粉残留在基底表面坑点中导致的,杂质在镀膜后析出,成为缺陷种子源。

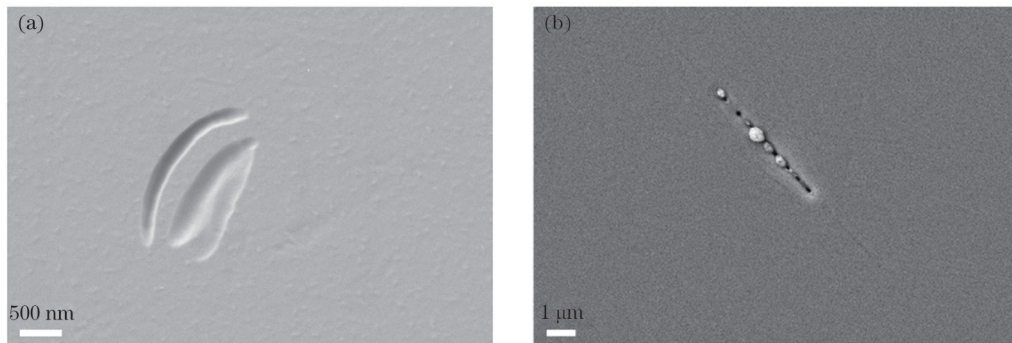


图 6 基底缺陷的 SEM 形貌图。(a) 坑点;(b) 高温退火后的基底裂纹

Fig. 6 SEM images of substrate defects. (a) Pit; (b) substrate crack after high temperature annealing

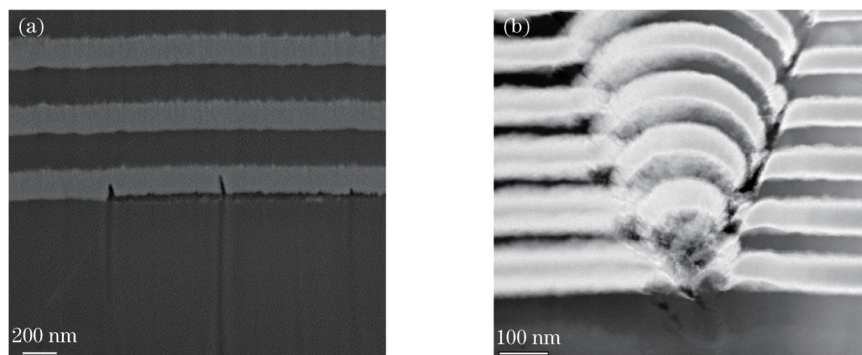


图 7 基底缺陷引起的膜层缺陷。(a) 薄膜底层剥离和孔隙的 SEM 图;(b) 膜层内的类节瘤缺陷结构的 TEM 图

Fig. 7 Film defects caused by substrate defects. (a) SEM image showing porosity and peeling of bottom layer of film; (b) TEM image of nodule-like defect structure in coatings

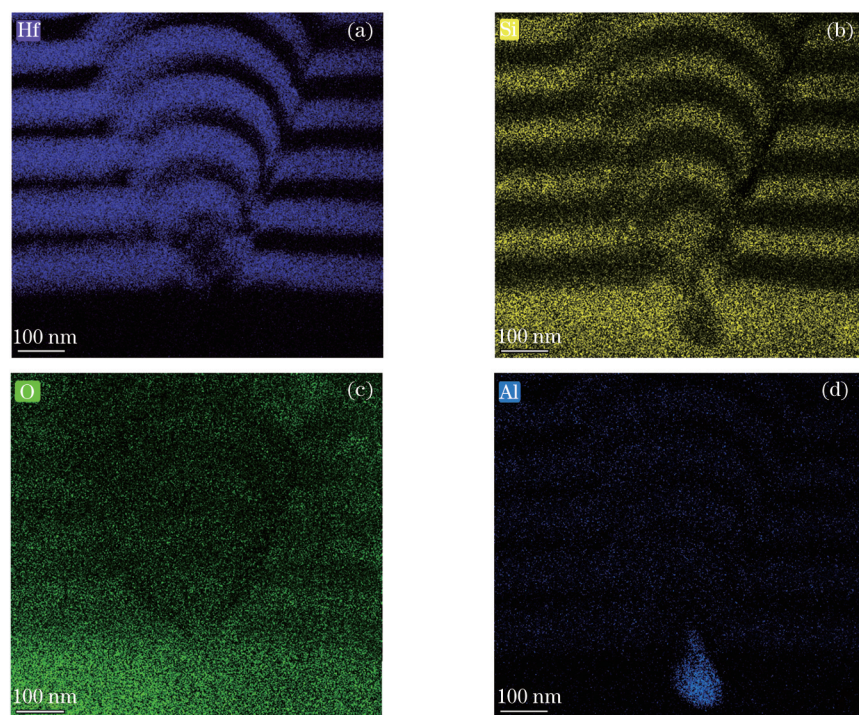


图 8 TEM-EDS 测得的图 7(b)中基底杂质的元素分布。(a)Hf;(b)Si;(c)O;(d)Al

Fig. 8 Element distributions of substrate impurities in Fig. 7(b) obtained by TEM-EDS. (a) Hf; (b) Si; (c) O; (d) Al

### 3.3 激光辐照微缺陷后的损伤特征

355 nm 高反射膜内的节瘤缺陷在激光辐照后产生的喷发损伤坑如图 9(a)所示,该点处的激光辐照能量密度为  $24.9 \text{ J/cm}^2$ 。对损伤坑进行局部放大,发现远离损伤坑的膜层致密,元素含量接近正常化学计量比,如图 9(b)所示;邻近损伤坑边缘的 H 层呈现明显的多孔

柱状结构,O 与 Hf 的原子数分数比明显低于 2:1,如图 9(c)所示;损伤坑底部和侧壁呈现熔融态,如图 9(d)所示,说明损伤区域的温升达到  $\text{HfO}_2$  和  $\text{SiO}_2$  的熔点。

532 nm 高反射膜在激光辐照后的裂纹状损伤坑如图 10(a)所示,该点处的激光辐照能量密度为  $82.7 \text{ J/cm}^2$ 。对损伤坑进行截面观察,发现损伤裂纹

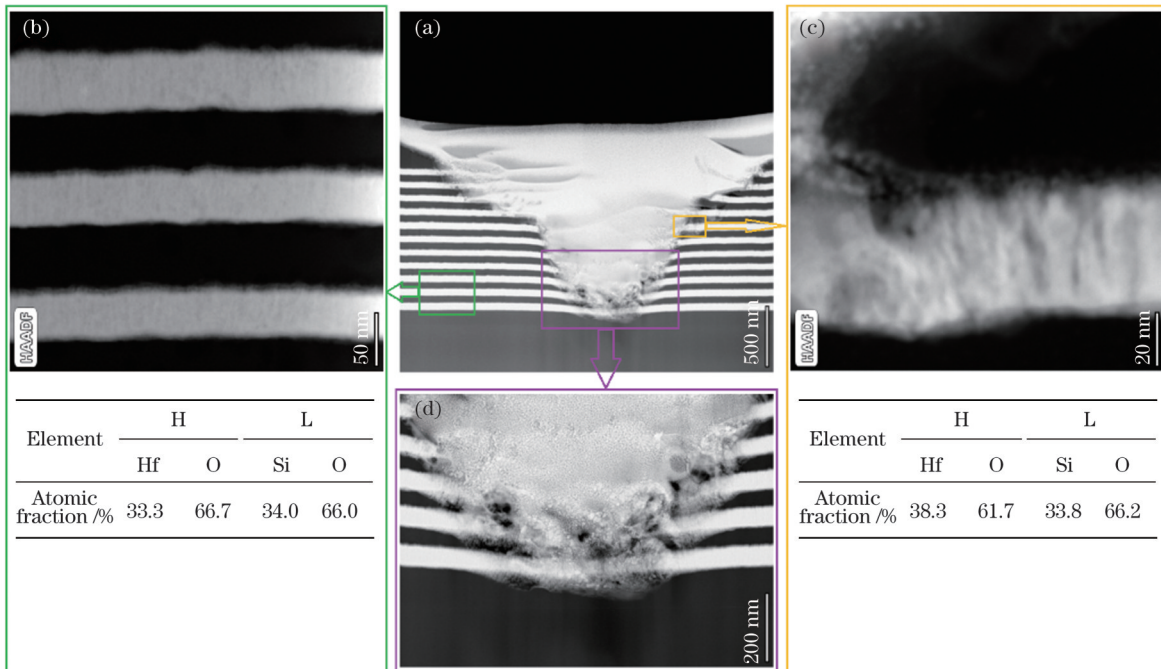


图 9 激光辐照后膜层内节瘤缺陷导致的喷发损伤坑的 TEM-EDS 分析。(a)损伤坑全貌;(b)远离损伤坑的膜层形貌及元素含量;(c)损伤坑边缘形貌及元素含量;(d)损伤坑底部形貌

Fig. 9 TEM-EDS analysis for sputter damage pit caused by nodule defect in film after laser irradiation. (a) Morphology of damage pit; (b) element content and morphology of film layer far away from damage pit; (c) element content and morphology of damage pit edge; (d) morphology of damaged pit bottom

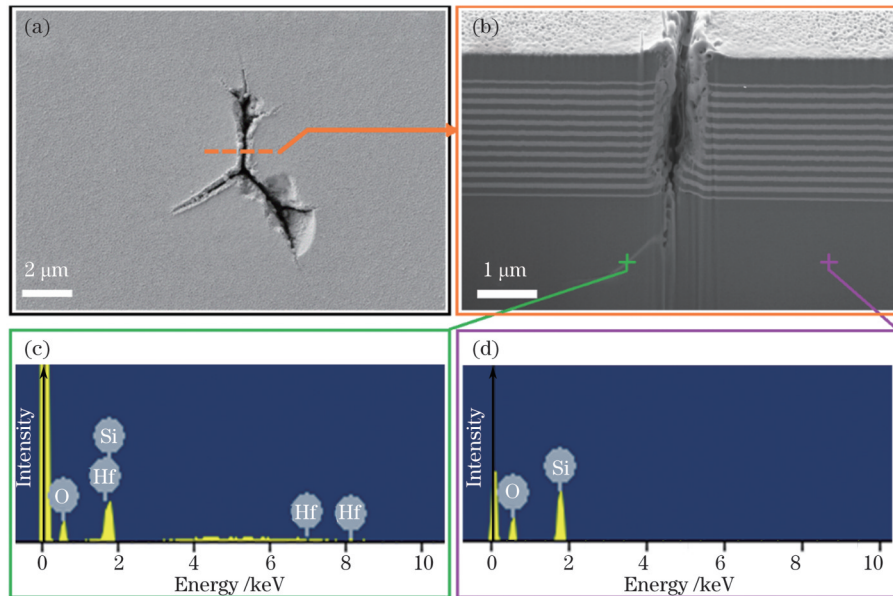


图 10 裂纹状损伤坑的 SEM-EDS 分析。(a)裂纹状损伤;(b)裂纹状损伤的截面形貌;(c)基底白色区域的元素;(d)基底非损伤区域的元素

Fig. 10 SEM-EDS analysis of crack-like damage pit. (a) Crack-like damage; (b) cross-sectional morphology of crack-like damage; (c) elements in white area of substrate; (d) elements in non-damaged area of substrate

延伸至基底较深处,且基底裂纹内有明显白色物质,如图 10(b)所示。对基底裂纹内的白色物质进行成分分析,并取同一水平位置处的非损伤区域作对比,测试结果如图 11(c)、(d)所示,白色区域含 Hf、Si 和 O 元素,非损伤区域仅含 Si 和 O 元素,而基底的主要成分为 Si 和 O。结果表明,缺陷在激光辐照后产生等离子体喷发的温度高于  $\text{HfO}_2$  气化温度( $5400^\circ\text{C}$ ),导致  $\text{HfO}_2$  气化进入基底裂纹中。

## 4 结 论

表征分析了基底及 355 nm 和 532 nm 高反膜元件表面的微缺陷来源及其损伤特征。通过对亚微米级缺陷点的三维重构,证明了其种子源为百纳米的喷溅  $\text{SiO}_2$  膜料。镀膜的真空加温过程会导致基底中 Na、K 离子的扩散并聚集于高折射率膜层;微米级膜料喷溅缺陷被激光辐照后生成的损伤坑边缘呈熔融状,邻近损伤坑边缘的  $\text{HfO}_2$  层呈明显多孔柱状结构,O 和 Hf 的原子数分数比低于 2:1;基底内的杂质缺陷被激光辐照后产生等离子体喷发的温度高于  $\text{HfO}_2$  气化温度,导致  $\text{HfO}_2$  气化进入基底裂纹。分析结果表明,为了提高激光损伤阈值,应进一步优化  $\text{SiO}_2$  预熔和沉积过程,避免百纳米的  $\text{SiO}_2$  缺陷;采用高纯度石英基底进行薄膜镀制;可采用离子束抛光技术去除传统抛光工艺带来的基底表面缺陷。

## 参 考 文 献

- [1] Spaeth M L, Wegner P J, Suratwala T I, et al. Optics recycle loop strategy for NIF operations above UV laser-induced damage threshold[J]. *Fusion Science and Technology*, 2016, 69(1): 265-294.
- [2] Stoltz C J. The National Ignition Facility: the path to a carbon-free energy future[J]. *Philosophical Transactions. Series A, Mathematical, Physical, and Engineering Sciences*, 2012, 370 (1973): 4115-4129.
- [3] Shao J D, Yi K, Zhu M P. Thin-film polarizer for high-power laser system in China[J]. *Proceedings of SPIE*, 2016, 9983: 998308.
- [4] Jeandet A, Borot A, Nakamura K, et al. Spatio-temporal structure of a petawatt femtosecond laser beam[J]. *Journal of Physics: Photonics*, 2019, 1(3): 035001.
- [5] Chen F, Ma J, Wei C, et al. 10 kW-level spectral beam combination of two high power broad-linewidth fiber lasers by means of edge filters[J]. *Optics Express*, 2017, 25(26): 32783-32791.
- [6] Jauregui C, Limpert J, Tünnermann A. High-power fibre lasers [J]. *Nature Photonics*, 2013, 7(11): 861-867.
- [7] Zhu M P, Zeng T T, Li J P, et al. Influence of deposition temperature and  $\text{SiO}_2$  overcoat layer on laser resistance of 532-nm high-reflection coating[J]. *Optical Engineering*, 2018, 57(12): 121902.
- [8] Negres R A, Stoltz C J, Batavićute G, et al. 532-nm, nanosecond laser mirror thin film damage competition[J]. *Proceedings of SPIE*, 2020, 11514: 115140L.
- [9] Stoltz C J, Negres R A. Ten-year summary of the Boulder Damage Symposium annual thin film laser damage competition[J]. *Optical Engineering*, 2018, 57(12): 121910.
- [10] Cheng X B, Zhang J L, Ding T, et al. The effect of an electric field on the thermomechanical damage of nodular defects in dielectric multilayer coatings irradiated by nanosecond laser pulses [J]. *Light: Science & Applications*, 2013, 2(6): e80.
- [11] 赵元安, 邵建达, 刘晓凤, 等. 光学元件的激光损伤问题[J]. 强激光与粒子束, 2022(1): 57-68.
- [12] Zhao Y A, Shao J D, Liu X F, et al. Tracking and understanding laser damage events in optics[J]. *High Power Laser and Particle Beams*, 2022(1): 57-68.
- [13] Grilli M L, Menchini F, Piegari A, et al.  $\text{Al}_2\text{O}_3/\text{SiO}_2$  and  $\text{HfO}_2/\text{SiO}_2$  dichroic mirrors for UV solid-state lasers[J]. *Thin Solid Films*, 2009, 517(5): 1731-1735.
- [14] Stoltz C J, Weng J G, Teklemarim T, et al. Evaluation of alumina and silica coating materials for the NIF final turning mirrors[J]. *Proceedings of SPIE*, 2021, 11910: 1191010.
- [15] DeShazer L G, Newnam B E, Leung K M. Role of coating defects in laser-induced damage to dielectric thin films[J]. *Applied Physics Letters*, 1973, 23(11): 607-609.
- [16] Cheng X B, Shen Z X, Jiao H F, et al. Laser damage study of nodules in electron-beam-evaporated  $\text{HfO}_2/\text{SiO}_2$  high reflectors[J]. *Applied Optics*, 2011, 50(9): C357-C363.
- [17] 单永光, 刘晓凤, 贺洪波, 等. 光学薄膜中节瘤缺陷研究进展[J]. 强激光与粒子束, 2011, 23(6): 1421-1429.
- [18] Shan Y G, Liu X F, He H B, et al. Research progress of nodular defect in optical coatings[J]. *High Power Laser and Particle Beams*, 2011, 23(6): 1421-1429.
- [19] Ma H P, Cheng X B, Zhang J L, et al. Electric-field intensity enhancement of a series of artificial nodules in a broadband high-reflection coating[J]. *Optical Engineering*, 2016, 56(1): 011027.
- [20] Qiu S R, Wolfe J E, Monterrosa A M, et al. Impact of substrate surface scratches on the laser damage resistance of multilayer coatings[J]. *Proceedings of SPIE*, 2010, 7842: 78421X.
- [21] Ma Z R, Lu Q, Liu H J, et al. Electric field enhancement effect of substrate surface scratches in 1064 nm high-reflection coating[J]. *Proceedings of SPIE*, 2021, 11912: 119120P.
- [22] Zou X, Kong F Y, Jin Y X, et al. Influence of nodular defect size on metal dielectric mixed gratings for ultra-short ultra-high-intensity laser system[J]. *Optical Materials*, 2019, 91: 177-182.
- [23] Bercegol H, Courchinoux R, Josse M A, et al. Observation of laser-induced damage on fused silica initiated by scratches[J]. *Proceedings of SPIE*, 2005, 5647: 78-85.
- [24] Miller P E, Suratwala T I, Wong L L, et al. The distribution of subsurface damage in fused silica[J]. *Proceedings of SPIE*, 2005, 5991: 599101.
- [25] Zhao Z C, Sun J, Zhu M P, et al. Research to improve the optical performance and laser-induced damage threshold of hafnium oxide/silica dichroic coatings[J]. *Optical Materials*, 2021, 113: 110890.
- [26] 杨明红, 赵元安, 单海洋, 等. 熔石英抛光表面结构的蚀刻和热处理表征[J]. 中国激光, 2012, 39(8): 0803004.
- [27] Yang M H, Zhao Y A, Shan H Y, et al. Surface structure features of polished fused silica revealed by etching and thermal treating[J]. *Chinese Journal of Lasers*, 2012, 39(8): 0803004.
- [28] Cui Y, Zhao J L, Zhao Y A, et al. Diffusion of metal ions from a substrate into oxide coatings[J]. *Optical Materials Express*, 2016, 6 (10): 3119-3126.
- [29] Cui Y, Zhao Y A, Zhang G, et al. Influence of annealing temperature on the performance of  $\text{TiO}_2/\text{SiO}_2$  nanolaminated films [J]. *Chinese Optics Letters*, 2021, 19(12): 121406.

# Characterization Analysis of Micro-defects in Thin-Film Components for Laser Systems

Cui Yun<sup>1,2\*</sup>, Zhang Ge<sup>1,2</sup>, Zhao Yuanan<sup>1,2</sup>, Shao Yuchuan<sup>1,2</sup>, Zhu Meiping<sup>1,2</sup>, Yi Kui<sup>1,2</sup>, Shao Jianda<sup>1,2\*\*</sup>

<sup>1</sup>Laboratory of Thin Film Optics, Shanghai Institute of Optics and Fine Mechanics, Chinese Academy of Sciences, Shanghai 201800, China;

<sup>2</sup>Key Laboratory of Materials for High Power Laser, Chinese Academy of Sciences, Shanghai 201800, China

## Abstract

**Objective** Thin-film components of laser systems require excellent optical performance and a high laser-induced damage threshold (LIDT). The micro-defects in the components (such as coating material ejection defects and substrate defects) are the critical cause for the reduced LIDT. To control micro-defects, we must first detect the defects and trace the formation process of micro-defects. In this study, the morphologies and structures of the micro-defects produced by coating and substrate polishing are characterized by precise cutting and three-dimensional reconstruction. Additionally, the element distributions before and after laser irradiation are analyzed. The results clarify the direction of the increasing LIDT of thin-film components.

**Methods** High-reflection films at 355 nm and 532 nm are deposited on BK7 substrates using the electron beam evaporation. The BK7 substrates are also used for surface topography measurements and additional measurements. Before deposition, the coating chamber is heated to 473 K and evacuated to a base pressure of  $1 \times 10^{-3}$  Pa. The deposition rates of HfO<sub>2</sub> and SiO<sub>2</sub> in the multilayer coatings are 0.1 nm/s and 0.2 nm/s, respectively. H and L represent the HfO<sub>2</sub> and SiO<sub>2</sub> layers with a quarter-wavelength optical thickness (QWOT) at 355 nm or 532 nm, respectively (Fig. 1).

The morphologies of the micro-defects are observed using focused ion beam scanning electron microscopy (FIB-SEM). The feature points are cut with an ion beam to obtain the cross-sectional morphology and structure, and the element composition in the designated area is analyzed using an energy dispersive spectrometer (EDS). Scanning transmission electron microscopy-high angle annular dark field (STEM-HAADF) images of the micro-defects are obtained using a 200 keV field emission transmission electron microscope (TEM). Three-dimensional reconstruction is conducted to analyze the submicron defects. Samples are prepared for the TEM observations using FIB-SEM. The LIDT is tested by 1-on-1. A  $2\omega$  Nd:YAG laser with a pulse width of 8 ns and a  $3\omega$  Nd:YAG laser with a pulse width of 8 ns are used for the 532 nm and 355 nm LIDT measurements, respectively. The effective beam sizes on the sample surface for the 532 nm and 355 nm LIDT measurements are approximately 0.32 mm<sup>2</sup> and 0.30 mm<sup>2</sup>, respectively. Ten sites are tested for each energy step.

**Results and Discussions** This study predominantly analyzes the micro-defects with the micron and sub-micron (hundred nanometers) scale. The morphologies and structures of the micro-defects produced by coating (Figs. 2 and 3) and substrate polishing (Figs. 6-8) are characterized by means of precise cutting and three-dimensional reconstruction, and the element distributions before and after laser irradiation are analyzed using EDS analysis. The results demonstrate that the seeds of submicron nodule defects arise from the ejection of SiO<sub>2</sub> during the deposition process (Figs. 4 and 5), whereby the seed diameter is 100 nm. The vacuum pumping and heating during the coating process cause the Na and K ions in the substrate to diffuse and concentrate in layers with a high refractive index (Fig. 5). Further, the seeds of micron-scale nodule defects originate from the ejection of SiO<sub>2</sub> or HfO<sub>2</sub> during the deposition process, whereby damaged pits are formed after the nodule defect is irradiated by laser, the edge of pits becomes molten, and the HfO<sub>2</sub> layer near the edge of the damaged pits has a prominent porous columnar structure, of which the atomic fraction ratio of O and Hf is less than 2:1 (Fig. 9). Impurity defects in the substrate produce plasma after being irradiated by laser, and the eruption temperature of the plasma is higher than the gasification temperature of HfO<sub>2</sub>, which causes the gasified HfO<sub>2</sub> to enter the substrate crack (Fig. 10).

**Conclusions** The results provide detailed data and evidence for improving coating and substrate polishing processes. The analysis results show that to improve the LIDT, the SiO<sub>2</sub> pre-melting and deposition process should be further optimized to avoid 100-nm SiO<sub>2</sub> defects, high-purity quartz substrates should be used to avoid the diffusion of metal ions in substrates, and ion beam polishing technology can be utilized to remove the substrate surface defects caused by traditional polishing processes.

**Key words** thin films; laser damage; microdefects; ejection; substrate polishing